analysis of the fragmentation data containing expected combinations of precursors **3** and **4**.

The coordination-driven self-assembly process described here facilitates the ready formation of single-molecule, highly symmetrical, static, non-dissociating ultrafine particles by simple mixing of predesigned, readily available components. This provides rapid access to supramolecular ensembles that are much larger than any classical synthetic macrocycles known at present. □

Methods

Preparation. A 5-ml round-bottom flask in a glovebox was charged either with 1,3,5-tris[4-(*trans*-Pt(PPh₃)₂OTf) phenylethynyl] benzene **1** (30 mg, 0.01 mmol) for cuboctahedron **5** or with bis(4-[*trans*-Pt(PPh₃)₃I]phenyl) ketone **2** (30 mg, 0.007 mmol) in 2 ml of CD_2Cl_2. Then, a solution of 4,4′-bispyridylacetal **3** (3.5 mg, 0.015 mmol) in 2 ml of CD_2Cl_2 was added dropwise to the solution of **1** or 1,3,5-tris(4′-pyridylethynyl)benzene **4** (3.2 mg, 0.011 mmol) was added to **2**, resulting in the solutions of cuboctahedrons **5** or **6**, respectively. The products were isolated by solvent removal *in vacuo*. Yields: 33.5 mg (99%) for **5** or 32 mg (98%) for **6**.

Characterization. The identity and purity of the products of self-assembly and their precursors was confirmed by ¹H, ³¹P{¹H}, ¹³C{¹H} and ¹⁹F NMR, IR, ESI-MS and elemental analyses: see Supplementary Information.

PGSE technique. A Stejscal-Tanner pulse sequence was used[13]. The diffusion coefficients for both **5** and **6** were determined using ³¹P resonances in dichloromethane-acetone mixtures at 25 °C on the Z-gradient probe capable of producing pulsed field gradients of nearly 200 G cm⁻¹. The molecular size was determined from the effective hydrodynamic radius R, related to the effective hydrodynamic volume V_m as $V_m = 4(\pi/3)R^3$. R is calculated from the Stokes–Einstein equation, $D = (k_B T)/(6\pi R\eta)$, where D is the diffusion coefficient, k_B is the Boltzmann constant, T is the absolute temperature, and η is the viscosity of the liquid through which the species is diffusing[14].

ESI-MS technique. Samples of **5** and **6** were dissolved in acetone (10–20 ng μl⁻¹) and injected via syringe pump (100-μl syringe) into a Micromass Quatro II mass spectrometer with ionization performed under electrospray conditions (flow rate, 7.7 μl min⁻¹; capillary voltage, 3.0 kV; cone, 47 V; extractor, 27 V). About 15 individual scans were averaged for the mass spectrum. The calibration of the mass range 500–3,000 atomic mass units was done with a 1:1 mixture of an isopropanol:water solution of NaI (2 μg μl⁻¹) and CsI (0.01 μg μl⁻¹). A table of ESI-MS data for **5** and **6** is available; see Supplementary Information.

1. Horne, R. W. *Virus Structure* (Academic, New York, 1974).
2. Lehn, J.-M., Atwood, J. L., Davis, J. E. D., MacNicol, D. D. & Vögtle, F. (eds) *Comprehensive Supramolecular Chemistry* Vol. I–II (Pergamon, Oxford, 1996).
3. Lehn, J.-M. *Supramolecular Chemistry: Concepts and Perspectives* (VCH, Weinheim, 1995).
4. Stoddard, J. F. (ed.) *Monographs in Supramolecular Chemistry* (Royal Society of Chemistry, Cambridge, 1989, 1991, 1994–1996).
5. Fujita, M. *et al.* Self-assembly of ten molecules into nanometre-sized organic host frameworks. *Nature* **378**, 469–471 (1995).
6. Cram, D. J. & Cram, J. M. *Container Molecules and Their Guests* (Royal Society of Chemistry, Cambridge, 1994).
7. Cram, D. J., Tanner, M. E. & Thomas, R. The taming of cyclobutane. *Angew. Chem. Int. Edn Engl.* **30**, 1024–1027 (1991).
8. Meissner, R. S., Mendoza, J. D. & Rebek, J. Jr Autoencapsulation through intermolecular forces: a synthetic self-assembling spherical complex. *Science* **270**, 1485–1488 (1995).
9. Kang, J. & Rebek, J. Jr Acceleration of a Diels-Alder reactions by a self-assembled molecular capsule. *Nature* **385**, 50–52 (1997).
10. Stang, P. J. & Olenyuk, B. Self-assembly, symmetry and molecular architecture: Coordination as the motif in the rational design of supramolecular metallacyclic polygons and polyhedra. *Acc. Chem. Res.* **30**, 502–518 (1997).
11. Persky, N. E., Manna, J. & Stang, P. J. Molecular architecture via coordination: Self-assembly of nanoscale platinum containing molecular hexagons. *J. Am. Chem. Soc. Soc.* **119**, 4777–4778 (1997).
12. Dinur, U. & Hagler, A. T. in *Reviews of Computational Chemistry II* (eds Lipkowitz, K. B. & Boyd, D. B.) Ch. 4 (VCH, New York, 1991).
13. Stejskal, E. O. & Tanner, J. E. Spin diffusion measurements: spin echoes in the presence of a time-dependent field gradient. *J. Chem. Phys.* **42**, 288–292 (1965).
14. Hansen, J. P. & McDonald, I. R. *Theory of Simple Liquids* (Academic, London, 1976).
15. Insight II 97.0 (Molecular Simulations Inc., San Diego, CA, 26 Jan 1998).

Correspondence and requests for materials should be addressed to P.J.S. (e-mail: stang@chemistry.chem.utah.edu).

Signature of recent climate change in frequencies of natural atmospheric circulation regimes

S. Corti*, **F. Molteni***‡ & **T. N. Palmer**†

* *CINECA-Interuniversity Computing Centre, Via Magnanelli 6/3, 40033 Casalecchio di Reno, Bologna, Italy*
† *European Centre for Medium-Range Weather Forecasts, Shinfield Park, Reading, RG2 9AX, UK*

A crucial question in the global-warming debate concerns the extent to which recent climate change is caused by anthropogenic forcing or is a manifestation of natural climate variability[1]. It is commonly thought that the climate response to anthropogenic forcing should be distinct from the patterns of natural climate variability. But, on the basis of studies of nonlinear chaotic models with preferred states or 'regimes', it has been argued[2,3] that the spatial patterns of the response to anthropogenic forcing may in fact project principally onto modes of natural climate variability. Here we use atmospheric circulation data from the Northern Hemisphere to show that recent climate change can be interpreted in terms of changes in the frequency of occurrence of natural atmospheric circulation regimes. We conclude that recent Northern Hemisphere warming may be more directly related to the thermal structure of these circulation regimes than to any anthropogenic forcing pattern itself. Conversely, the fact that observed climate change projects onto natural patterns cannot be used as evidence of no anthropogenic effect on climate. These results may help explain possible differences between trends in surface temperature and satellite-based temperature in the free atmosphere[4–6].

Our climate can be thought of as a nonlinear dynamical system with a chaotic attractor. Let us imagine that the anthropogenic influence on climate (for example, from increased atmospheric concentration of CO_2) can be represented by a weak imposed forcing on this dynamical system. Because of the nonlinearity of the underlying system, its sensitivity to this forcing will vary with location on the attractor; in regions of strong local instability[7] the system may be sensitive to the imposed forcing, but in regions of stability the system will be relatively insensitive. This notion can be demonstrated on the chaotic Lorenz[8] system which has two dominant regimes. Irregular fluctuations between these regimes characterize the model's principal mode of internal variability. Largely independent of the details of the imposed forcing, the response of the Lorenz system to an imposed forcing is associated with an increase in the probability density function (PDF) associated with one regime, and a decrease in the PDF associated with the other regime (Fig. 1). (In the unforced Lorenz model, the PDF has the same value at both centroids.) By contrast, the locations of the regimes' centroids in phase space are largely unaffected by the imposed forcing. This can be understood by noting that the centroids of the regimes are phase-space regions of relative stability; the system is sensitive to the imposed forcing in a region of the attractor between the two centroids.

If this picture were applicable to the real climate system, it would imply that anthropogenically forced changes in climate would project primarily onto the principal patterns of natural variability, even though such natural variability may occur predominantly on

‡ Present address: The Abdus Salam International Centre for Theoretical Physics, PO Box 586, 34100 Trieste, Italy.

timescales much shorter than that of the imposed forcing.

To validate this approach, we performed a study on monthly-mean objective analyses of Northern Hemisphere (NH) extended-winter (November to April) 500-hPa geopotential height—essentially the height of a constant pressure surface in the mid-troposphere—from the US National Centers for Environmental Prediction (NCEP), from 1949 to 1994, on a regular latitude/longitude grid with 2.5-degree spacing. First, the seasonal cycle has been removed from the data by computing anomalies with respect to the long-term monthly mean. Second, the data is further detrended by taking deviations from a 5-year running mean. An empirical orthogonal function (EOF) analysis is then applied to this detrended data in order to define a reduced phase space based on patterns of variability with timescales shorter than the observed decadal trends. The resulting EOFs are very similar to those shown in ref. 9, and are not shown here for brevity. (The structure of the EOFs can also be deduced from the PDF maxima shown below.) Whilst the first two EOFs only explain 27% of monthly mean variance (32% of 5-year mean variance), as discussed below, their significance lies in the fact that their spatial structure is well correlated with recent climate-change patterns.

Each panel in Fig. 2 shows a PDF of the projection coefficients of the non-detrended monthly mean height field, in the reduced phase space spanned by the first two detrended EOFs. These PDFs have been generated using a gaussian-kernel estimator[10], with a smoothing parameter large enough to detect multimodality with statistical significance. Figure 2a shows the PDF for the whole period (1949–94). There are four maxima, labelled A, B, C, D in Fig. 2a. Consistent with earlier studies[9,11,12], the presence of these maxima confirms that the PDF of the climate attractor is multimodal, and therefore cannot be described adequately using a multinormal distribution. The geographical patterns of these density maxima are illustrated in Fig. 3, where they are shown as departures from the 1949–94 mean 500-hPa height.

Cluster A (Fig. 3) is a regime whose spatial structure is very similar to the pattern found by linear regression analysis between monthly-mean NH-mean surface air temperature and 500-hPa height (compare cluster A with Figure 5 in ref. 13). Essentially, this pattern denotes the manifestation in 500-hPa geopotential height of the "cold ocean warm land" (COWL) pattern, which, to a first approximation, describes much of the recent climate change of NH surface air temperature[1,13]. Hence, although cluster A is
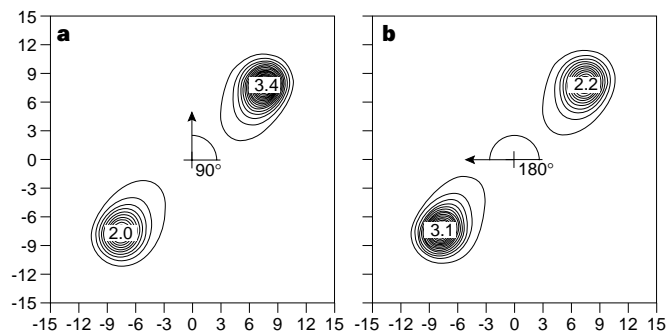
defined from intraseasonal and interannual variations, a NH-mean surface temperature warming trend would be consistent, in the nonlinear approach, with an increase in residence frequency of cluster A. The height anomalies associated with clusters B and C (Fig. 3) have projection onto the negative Pacific North American[14] (PNA) pattern. The existence of multiple regimes with negative PNA index is consistent with studies[11,15] showing relatively high intraseasonal variability during periods of negative PNA-index circulation. Cluster B has a projection onto the positive North Atlantic Oscillation[16] patterns, whilst cluster D (Fig. 3) shows a pattern with most amplitude over the North Atlantic, extending over the Arctic. In fact, cluster D is extremely well correlated with the 500-hPa height component of the so-called Arctic Oscillation[17] in its negative phase.

The nonlinear picture outlined above applies to anomalous forcing from the ocean, as well as to anthropogenic forcing. Hence, in one test of the approach, we recomputed the two-dimensional PDF from the NCEP data, with all El Niño/La Niña years removed (using the stratification proposed in ref. 18). This results in 13 warm El Niño years and 7 cold La Niña years being removed from the data: results are shown in Fig. 2b. It can be seen that the four clusters of Fig. 2a continue to be observed in the reduced data set; in other words, none of the regimes A–D owes its existence to forcing by El Niño. However, El Niño does affect the regime frequencies; most noticeably, the frequency of occurrence of cluster A (associated with the COWL pattern) is reduced. The ability of El Niño to excite a response pattern similar to cluster A has been noted elsewhere[3,19]. The reduction in the PDF of cluster A is
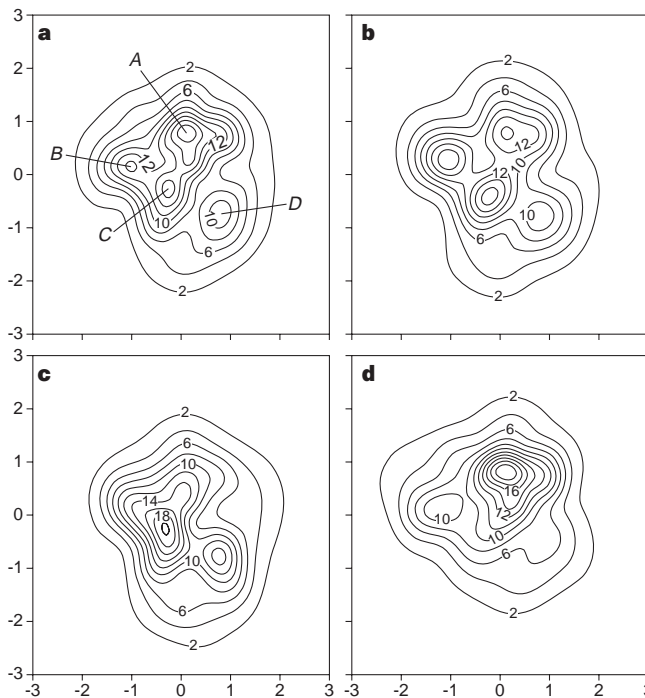

Figure 2 Evidence of recent change in the climate attractor. Illustrated is the atmospheric state vector PDF based on monthly-mean 500-hPa geopotential height in the space spanned by the two dominant atmospheric EOFs computed from detrended monthly mean timeseries. See text for details. **a**, Using all data from the 1949–94 period. See text for details about maxima A, B, C, D. **b**, Using data from the 1949–94 period, from which all months in which El Niño/ La Niña events occurred, have been removed. **c**, Using data from the 1949–71 sub-period. **d**, Using data from the 1971–94 sub-period. The quantities plotted on the horizontal and vertical axes are projection coefficients of geopotential height onto the first and second EOFs respectively. We note that the same detrended EOFs are used in all four panels, hence the origin refers to the same atmospheric state in each panel.

Figure 1 Response of a nonlinear chaotic model to imposed forcing. Illustrated is the state vector PDF (invariant measure) of a forced Lorenz[3] attractor, with governing equations $\dot{X} = -10X + 10Y + 2.5\cos\theta$, $\dot{Y} = -XZ + 28X - Y + 2.5\sin\theta$, $\dot{Z} = XY - (8/3)Z$, in X, Y phase space. The arrow shown is the forcing vector $(2.5\cos\theta, 2.5\sin\theta)$ in this two-dimensional phase space. A short running time-average has been applied to the state vector to emphasise the regime character of the Lorenz attractor. **a**, $\theta = 90°$; **b**, $\theta = 180°$. The numbers shown correspond to maxima of the PDF at the regime centroids. The quantities plotted on the horizontal and vertical axes are values of X and Y respectively. See ref. 3 for details.

consistent with the removal of more warm El Niño events than cold La Niña events from the full data set.

We now return to the changes in the PDF on decadal timescales. PDFs for the sub-periods 1949–71 and 1971–94 are shown in Fig. 2c and d, respectively. It can be seen that in the first-half period, the PDF associated with cluster A is reduced (compared with long-term values), whilst the PDFs associated with clusters C and D are enhanced. In the second-half period, on the other hand, the PDF associated with cluster A is strongly enhanced, whilst the PDFs associated with all the other clusters are reduced. Comparing Fig. 2c and d with Fig. 2a, it can be seen that the phase-space location of the regimes is relatively stable despite these large changes in the PDF.

The decrease in the PDF of cluster D in the second-half period is consistent with what has been noted[17] as a "systematic bias in one of the atmosphere's dominant naturally-occurring modes of variability". On the basis of the approach presented here, it is possible that this bias is a response to anthropogenic forcing (recent model integrations confirm a strong effect of anthropogenic forcing on the Arctic Oscillation[25]).

The changes in the PDF of the climate attractor are consistent with more conventional analyses of recent climate change. For example, in Fig. 4 we show the time series of the projection coefficients of the non-detrended height anomalies onto the first and second detrended EOFs. Both seasonal and 10-year running mean filters have been applied to the time series of the monthly-mean coefficients. The time series from the second EOF shows a clear upward trend, consistent with the increase in the frequency of cluster A (which, from its position in the reduced phase space of Fig. 2, can be described almost exactly in terms of the second EOF pattern). In fact, much of the recent climate-change signal can be explained in terms of this detrended EOF. If Δ denotes the difference field between the 1949–71 time-mean geopotential height and the 1971–94 time-mean geopotential height, and $P_2(\Delta)$ denotes the projection of Δ onto the second detrended

EOF, then the spatial correlation between Δ and $P_2(\Delta)$ is 0.6. In contrast, there is no clear trend in the timeseries from the first EOF; however, the evidence of decreased values towards the end of the period is consistent with a decrease in the frequency of occurrence of cluster D (and a corresponding increase in the Arctic Oscillation index).

Overall, our results indicate that in the NH, much of the recent tropospheric climate change can be understood in terms of a change in the frequency of residence of dominant, naturally occurring regimes of NH atmospheric intraseasonal-interannual variability, consistent with the nonlinear approach outlined above. Although the regime structure of the real climate attractor is certainly more complex than the two-regime Lorenz attractor, observed climate change is qualitatively consistent with the simple picture outlined in Fig. 1.

This study has a number of implications. First, we note that just because the geographical distribution of observed climate change correlates well with patterns of natural variability, this cannot be taken to imply an absence of anthropogenic forcing.

Second, the increase in hemispheric-mean temperature in recent years is, in part at least, directly associated with an increase in the frequency of the cluster-A circulation regime. From this point of view, to attribute the observed hemispheric mean surface warming to a direct forcing by the "greenhouse effect" is an oversimplification. If this regime-induced climate change is anthropogenic, then a relevant question is: why should increased CO_2 lead to an increase in the frequency of cluster A? To answer it, one should take into account the fact that large-scale atmospheric patterns are much
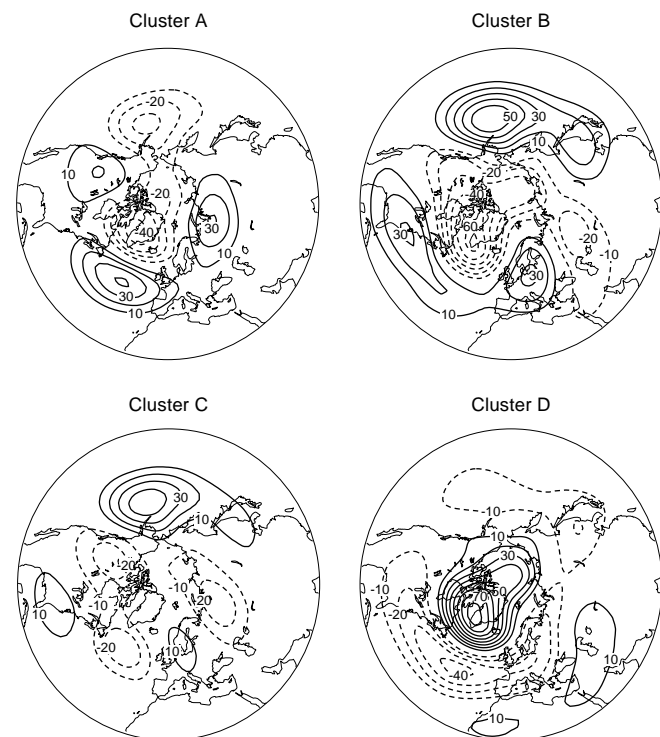

Figure 3 Geographical patterns of the four atmospheric regimes. Shown is the geographical distribution of 500-hPa geopotential height anomaly associated with clusters A (The "cold ocean warm land" regime) B, C and D (the "Arctic Oscillation" regime). Contour interval, 10 m.
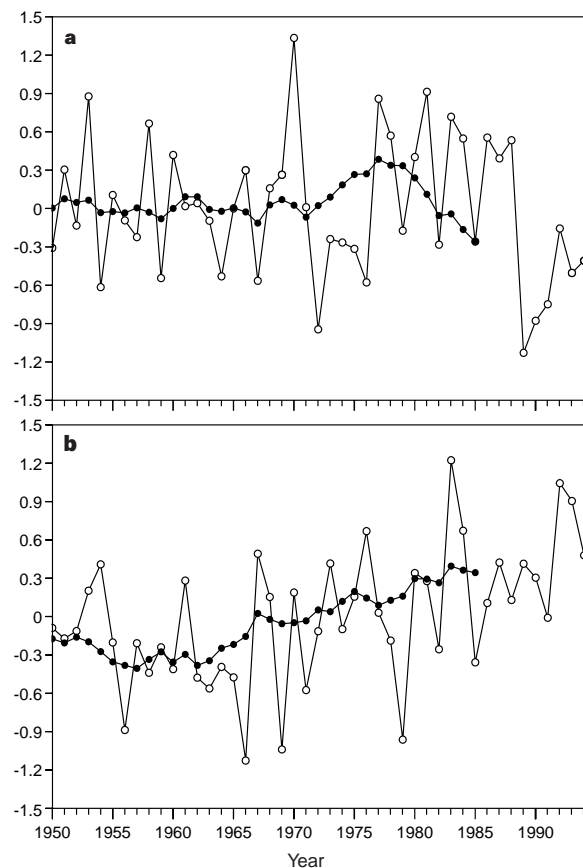

Figure 4 Evidence of climate trends. Shown are time series (1949–94) of the projection coefficients of non-detrended objective analyses of 500-hPa geopotential height onto the two dominant detrended EOFs of 500hPa geopotential height. Open circles, seasonal averages; filled circles, decadal averages. **a**, Projection coefficient of first EOF. **b**, Projection coefficient of second EOF.

more sensitive to some forcing perturbations than to others. Moreover, because of the non-normality of the relevant dynamical operators[20–22], changes in regime frequency will be sensitive to forcing perturbations which may have little spatial correlation with the regimes themselves. Different approaches, all based on adjoint dynamical methods, have been proposed[20–22] to investigate the structure of these sensitive patterns and their 'optimal' forcing fields, either in a stationary or in a time-dependent framework. At present, we do not have a satisfactory understanding of these regime instabilities, and how anomalous radiative forcing projects on the sensitivity patterns.

Third, if the horizontal structure of recent climate change is correlated with the horizontal structure of regimes of natural variability, then, by implication, the same should be true of the vertical structure: specifically, the vertical temperature profile of observed climate change should reflect the vertical temperature profile of the regimes, rather than the vertical structure of any perturbed radiative forcing. Away from the surface layer, temperature anomalies associated with cluster A will be similar in magnitude over sea and over land. However, at the surface, temperature anomalies associated with cluster A will be larger over the land than over the sea, because of the smaller heat capacity of the land surface. Hence the hemispheric-mean temperature anomaly associated with cluster A will be weaker in the free atmosphere than in the surface layer. The signal, however strong or weak it is, should reverse at the level of maximum geopotential anomaly, that is, at about the 300-hPa level. This is consistent with satellite observations in the free atmosphere[4,5] in spite of the implications of orbital decay[6]. A more complete resolution of this question requires an analysis of the three-dimensional structure of these circulation regimes; the so-called reanalysis datasets[23] would be well-suited for this task.

Last we note that these results indicate that predictions of anthropogenic climate change require models which can simulate accurately natural circulation regimes and their associated variability, even though the dominant timescale of such variability may be much shorter than the climate-change signal itself. More generally, these models should be able to simulate the non-gaussian characteristics of the climate attractor. As yet, few tests have been performed on climate models to assess this component of their behaviour[24]. □

1. Houghton, J. T. *et al.* (eds) *Climate Change 1995: The Science of Climate Change* (Cambridge Univ. Press, 1996).
2. Palmer, T. N. A nonlinear dynamical perspective on climate change. *Weather* **48**, 313–348 (1993).
3. Palmer, T. N. A nonlinear dynamical perspective on climate prediction. *J. Clim.* **12**, 575–591 (1999).
4. Christy, J. R. & McNider, R. T. Satellite greenhouse signal. *Nature* **367**, 325 (1994).
5. Hurrell, J. W. & Trenberth, K. E. Difficulties in obtaining reliable temperature trends: reconciling the surface and satellite microwave sounding units records. *J. Clim.* **11**, 945–967 (1998).
6. Wentz, F. J. & Schabel, M. Effects of orbital decay on satellite-derived lower-tropospheric temperature trends. *Nature* **394**, 661–664 (1998).
7. Abarbanel, H. D. I., Brown, R. & Kennel, M. B. Variation of Lyapunov exponents on a strange attractor. *J. Nonlin. Sci.* **1**, 175–199 (1991).
8. Lorenz, E. N. Deterministic nonperiodic flow. *J. Atmos. Sci.* **20**, 130–141 (1963).
9. Kimoto, M. & Ghil, M. Multiple flow regimes in the northern hemisphere winter. Part I: Methodology and hemispheric regimes. *J. Atmos. Sci.* **50**, 2625–2643 (1993).
10. Silverman, B. W. *Density Estimation for Statistics and Data Analysis* (Chapman & Hall, New York, 1986).
11. Molteni, F., Tibaldi, S. & Palmer, T. N. Regimes in the wintertime circulation over northern extratropics. I: Observational evidence. *Q. J. R. Meteorol. Soc.* **116**, 31–67 (1990).
12. Cheng, X. & Wallace, J. M. Cluster analysis of the Northern Hemisphere wintertime 500-hPa height field: spatial patterns. *J. Atmos. Sci.* **50**, 2674–2696 (1993).
13. Wallace, J. M., Zhang, Y. & Bajuk, L. Interpretation of interdecadal trends in Northern Hemisphere surface air temperature. *J. Clim.* **9**, 249–259 (1996).
14. Wallace, J. M. & Gutzler, D. S. Teleconnections in the geopotential height field during the northern hemisphere winter. *Mon. Weath. Rev.* **109**, 784–812 (1981).
15. Palmer, T. N. Medium and extended range predictability, and stability of the PNA mode. *Q. J. R. Meteorol. Soc.* **114**, 691–713 (1988).
16. Hurrell, J. W. Decadal trends in the North Atlantic Oscillation: regional temperature and precipitation. *Science* **269**, 676–679 (1995).
17. Thompson, D. W. J. & Wallace, J. M. The Arctic Oscillation signature in the wintertime geopotential height and temperature fields. *Geophys. Res. Lett.* **25**, 1297–1300 (1998).
18. Renwick, J. A. & Wallace, J. M. Relationships between North Pacific blocking, El Nino and the PNA pattern. *Mon. Weath. Rev.* **124**, 2071–2076 (1996).
19. Molteni, F., Ferranti, L., Palmer, T. N. & Viterbo, P. A dynamical interpretation of the global response to equatorial Pacific SST anomalies. *J. Clim.* **6**, 777–795 (1993).
20. Marshall, J. & Molteni, F. Towards a dynamical understanding of planetary-flow regimes. *J. Atmos. Sci.* **50**, 1792–1818 (1993).
21. Farrell, B. F. & Ioannou, P. J. Generalised stability theory: Part II: Nonautonomous systems. *J. Atmos. Sci.* **53**, 2042–2053 (1996).
22. Corti, S. & Palmer, T. N. Sensitivity analysis of atmospheric low-frequency variability. *Q. J. R. Meteorol. Soc.* **123**, 2425–2447 (1997).
23. Bengtsson, L. & Shukla, J. Integration of space and in situ observations to study global climate change. *Bull. Am. Meteorol. Soc.* **69**, 1130–1143 (1988).
24. Hannachi, A. Low-frequency variability in a GCM: Three-dimensional flow regimes and their dynamics. *J. Clim.* **10**, 1357–1379 (1997).
25. Shindell, D. T., Miller, R. L., Schmidt, G. A. & Pandolfo, L. Simulation of recent northern winter climate trends by greenhouse-gas forcing. *Nature* (in the press).

Methane-consuming archaebacteria in marine sediments

Kai-Uwe Hinrichs*, **John M. Hayes***, **Sean P. Sylva***, **Peter G. Brewer**† & **Edward F. DeLong**†

* *Woods Hole Oceanographic Institution, Woods Hole, Massachusetts 02543, USA*
† *Monterey Bay Aquarium Research Institute, Moss Landing, California 95039, USA*

Large amounts of methane are produced in marine sediments but are then consumed before contacting aerobic waters or the atmosphere[1]. Although no organism that can consume methane anaerobically has ever been isolated, biogeochemical evidence indicates that the overall process involves a transfer of electrons from methane to sulphate and is probably mediated by several organisms, including a methanogen (operating in reverse) and a sulphate-reducer (using an unknown intermediate substrate)[2]. Here we describe studies of sediments related to a decomposing methane hydrate. These provide strong evidence that methane is being consumed by archaebacteria that are phylogenetically distinct from known methanogens. Specifically, lipid biomarkers that are commonly characteristic of archaea are so strongly depleted in carbon-13 that methane must be the carbon source, rather than the metabolic product, for the organisms that have produced them. Parallel gene surveys of small-subunit ribosomal RNA (16S rRNA) indicate the predominance of a new archael group which is peripherally related to the methanogenic orders Methanomicrobiales and Methanosarcinales.

We investigated sediments from a methane seep in the Eel River basin, offshore northern California ($40°\,47.08′$ N, $124°\,35.30′$ W), an area with abundant methane hydrates at temperature–pressure conditions near their threshold of stability[3]. We combined a process-oriented investigation of abundances of ^{13}C in individual biomarkers[4] with culture-independent molecular phylogenetic surveys (see Methods)[5]. Hydraulic piston cores of sediments at a water depth of 521 m were retrieved by the ROV *Ventana*, operated by the Monterey Bay Aquarium Research Institute. Two seep-related samples (HPC 4, at a depth of 22 cm below the sediment surface; PC 26, 13–15 cm) and one control sample that was not near any active seeps (HPC 5, 33–36 cm) were examined. At the seep, methane bubbling into the water column is slightly enriched in ^{13}C (δ^{13}C = -49.5‰ relative to VPDB standard; K. Kvenvolden, unpublished data) relative to near-surface hydrates in the same region (-57.6 to -69.1‰; ref. 3). The organic matter extracted from the seep sediments contains less ^{13}C than the control sample (PC 26, -33‰; HPC 5, -26.8‰), presumably because products of methane-oxidizing organisms have accumulated within the microbial community.